Title

Acrylamide fragment inhibitors that induce unprecedented conformational distortions in enterovirus 71 3C and SARS-CoV-2 main protease.

Journal

Acta Pharmaceutica Sinica B, 12(10)

ISSN

2211-3835

Authors

Qin, Bo
Craven, Gregory
Hou, Pengjiao
et al.

Publication Date

2022-10-01

DOI

10.1016/j.apsb.2022.06.002

Peer reviewed

Acta Pharmaceutica Sinica B 2022;12(10):3924–3933

Chinese Pharmaceutical Association
Institute of Materia Medica, Chinese Academy of Medical Sciences

Acta Pharmaceutica Sinica B

www.elsevier.com/locate/apsb
www.sciencedirect.com

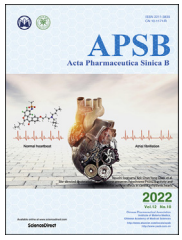

ORIGINAL ARTICLE

Acrylamide fragment inhibitors that induce unprecedented conformational distortions in enterovirus 71 3C and SARS-CoV-2 main protease

Bo Qin[a,†], Gregory B. Craven[b,†], Pengjiao Hou[a,†], Julian Chesti[c], Xinran Lu[c], Emma S. Child[b], Rhodri M.L. Morgan[b], Wenchao Niu[d], Lina Zhao[d], Alan Armstrong[c], David J. Mann[b,*], Sheng Cui[a,*]

[a]*NHC Key Laboratory of Systems Biology of Pathogens, Institute of Pathogen Biology, Chinese Academy of Medical Sciences & Peking Union Medical College, Beijing 100076, China*
[b]*Department of Life Sciences, Imperial College London, South Kensington Campus, London SW7 2AZ, UK*
[c]*Department of Chemistry, Imperial College London, Molecular Sciences Research Hub, White City Campus, Wood Lane, London W12 0BZ, UK*
[d]*CAS Key Laboratory for Biomedical Effects of Nanomaterials and Nanosafety, Institute of High Energy Physics, University of Chinese Academy of Sciences, Beijing 100049, China*

Received 26 February 2022; received in revised form 26 May 2022; accepted 1 June 2022

KEY WORDS

SARS-CoV-2;
Protease inhibitors;
Covalent fragments;
Allosteric inhibition;
EV71

Abstract RNA viruses are critically dependent upon virally encoded proteases to cleave the viral polyproteins into functional proteins. Many of these proteases exhibit a similar fold and contain an essential catalytic cysteine, offering the opportunity to inhibit these enzymes with electrophilic small molecules. Here we describe the successful application of quantitative irreversible tethering (qIT) to identify acrylamide fragments that target the active site cysteine of the 3C protease ($3C^{pro}$) of Enterovirus 71, the causative agent of hand, foot and mouth disease in humans, altering the substrate binding region. Further, we re-purpose these hits towards the main protease (M^{pro}) of SARS-CoV-2 which shares the 3C-like fold and a similar active site. The hit fragments covalently link to the catalytic cysteine of M^{pro} to inhibit its activity. We demonstrate that targeting the active site cysteine of M^{pro} can have profound allosteric effects, distorting secondary structures to disrupt the active dimeric unit.

*Corresponding authors. Tel./fax: +86 10 67828669 (Sheng Cui); +44 20 75945302 (David J. Mann).
E-mail addresses: D.mann@imperial.ac.uk (David J. Mann), cui.sheng@ipb.pumc.edu.cn (Sheng Cui).
[†]These authors made equal contributions to this work.
Peer review under responsibility of Chinese Pharmaceutical Association and Institute of Materia Medica, Chinese Academy of Medical Sciences

https://doi.org/10.1016/j.apsb.2022.06.002

1. Introduction

RNA viruses cause significant morbidity and mortality in human and animal hosts[1,2]. For example, enteroviruses (EV) include many important human pathogens with the best characterized being enterovirus 71 (EV71), rhinovirus (HRV), coxsackievirus B3 (CVB3), enterovirus D68 (EV-D68) and poliovirus (PV). EV71 is one cause of hand, foot and mouth disease (HFMD) in humans and is associated with severe neurological disease with considerable mortality[3]. Vaccines against EV71 have been developed and approved[4] but outbreaks persist and there are no antiviral drugs available for treating EV71[5,6].

Like many other RNA viruses, EV71 relies on proteases to cleave a polyprotein precursor into individual functional mature proteins. For enteroviruses, the majority of this proteolytic processing utilizes the 3C protease ($3C^{pro}$)[7]. Given the essential role of virally-encoded proteases in viral life-cycles, numerous protease inhibitors have been developed for potential clinical use[8]. These include a large collection of picornaviral $3C^{pro}$ inhibitors, such as an HRV $3C^{pro}$ inhibitor Rupintrivir (AG7088)[9] that failed to show patient benefit in phase II clinical trials[10]. To date, no $3C^{pro}$ inhibitors have been approved for clinical use.

With the global rise of SARS-CoV-2, scientific attention has focused on the causative agent, SARS-CoV-2[11]. At the end of 2021, the emergence of the heavily mutated omicron variant of SARS-CoV-2 (B.1.1.529) put the world on alert. This variant is classified as the fifth variant of concern (VOC) for its alarming transmissibility, high risk of reinfection and reduction in vaccine protection against the variant[12]. Whereas a large number of mutations of omicron variant concentrate on the spike protein, most of its nonstructural proteins involved in replication remains conserved. SARS-CoV-2 expresses two precursor polyproteins (pp1a and pp1ab) that are cleaved by both main protease (M^{pro})[13] and papain-like protease (PL^{pro})[14]. Interestingly, M^{pro} and $3C^{pro}$ share a similar fold and active site architecture, both proteases being absolutely reliant on the catalytic cysteine for activity[14]. Exploiting these structural similarities may enable identification of pharmacophores that target a wide variety of viral proteases.

Therapeutics with a covalent mechanism of action are becoming more widely accepted for a range of diseases[15]. Targeted covalent therapeutics such as ibrutinib[16] and osimertinib[17] use a Michael acceptor to react with the thiolate of cysteine, giving irreversible target engagement[18]. Identifying the starting points for such agents is often the bottleneck in development. Fragment-based approaches offer an efficient starting point and have already shown significant promise in targeting SARS-CoV-2 M^{pro}[19]. We have recently developed quantitative irreversible tethering (qIT), a high-throughput method for identifying selective covalent fragments that bind to a desired cysteine on a target protein[20]. qIT enables hit prioritization and minimization of false positives and negatives through normalization of the rate of protein modification by compound intrinsic reactivity[21].

Of note, the US Food and Drug Administration recently authorizes a Pfizer's COVID-19 treatment, Paxlovid, that is ~89% effective in preventing hospitalization[22]. A major component of Paxlovid is the compound PF-07321332. PF-07321332 covalently binds the active site of SARS-CoV-2 M^{pro} through a nitrile warhead[23], exemplifying successful use of covalent inhibitor for antiviral treatment. Here we employ qIT to identify inhibitory fragments that covalently target the active site cysteine of EV71 $3C^{pro}$. Co-crystals of 3C-fragment complexes demonstrated the occupancy of a novel, cryptic pocket in $3C^{pro}$. Furthermore, when repurposed towards M^{pro}, the covalent fragments also preferentially targeted the active site cysteine, inhibiting the enzyme activity and, in one case, additionally disrupting the quaternary structure of M^{pro}.

2. Results and discussion

2.1. Covalent fragment screening against EV71 $3C^{pro}$ by quantitative irreversible tethering (qIT)

To target cysteine C147 on EV71 $3C^{pro}$, we constructed a 1040-member covalent fragment library using a combination of in-house parallel synthesis and commercial vendors (Fig. 1A and B). Fragment-like core scaffolds were functionalized with cysteine-reactive chemical groups, with the majority (>95%) being acrylamides. Acrylamide "warheads" are featured in several clinically approved covalent drugs and are favored for their mild electrophilic reactivity, minimizing potential non-specific reactivity and associated toxicity[24]. In line with the generally accepted fragment-based drug design (FBDD) guidelines, the library was designed to maximize scaffold diversity and to conform to the "rule of 3"[25]: MW $<$ 300, *c*log*P* $\leq$ 3, H-bond donors/acceptors $\leq$3 (Fig. 1C).

We applied our fluorescence-based covalent fragment screening platform (qIT) to identify fragments which covalently bind to C147 on EV71 $3C^{pro}$ (Fig. 2A). To determine the rate of reaction between a cysteine thiol and an acrylamide fragment, the cysteine quantification probe CPM is employed to measure the degree of cysteine modification at a series of timepoints. The CPM probe competes with the acrylamide for modification of the cysteine residue such that the fluorescence signal is inversely proportional to the extent of acrylamide-cysteine labelling, allowing the rate of reaction (v) to be determined by exponential regression analysis in high-throughput. Our workflow uses GSH as a control cysteine-containing biomolecule and hit fragments are those that react significantly faster with $3C^{pro}$ than with GSH (Fig. 2B). The selectivity of the fragment towards the $3C^{pro}$ is quantified by the rate enhancement factor (REF) which was used to identify and prioritize hit fragments (Fig. 2C).

The 1040-member acrylamide fragment library was screened at 500 μmol/L against EV71 $3C^{pro}$ (5 μmol/L) or GSH (5 μmol/L) in parallel and the fluorescence intensity measured over 24 h. The majority of the library (61%) displayed measurable reactivity with EV71 $3C^{pro}$ over the 24-h time course, with roughly half of those fragments showing selectivity over GSH (REF >1) (Fig. 3A). There were 13 fragments which had a REF greater than three standard deviations (1SD = 2.5) over the geometric mean

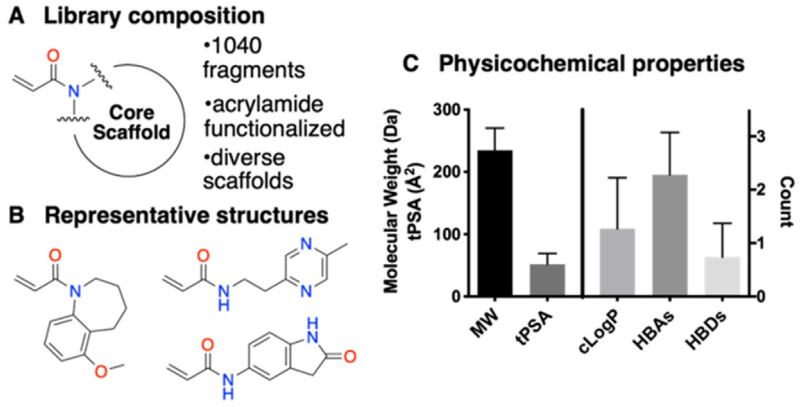

Figure 1 Cysteine-reactive covalent fragment library composition. (A) Covalent fragment library composition. (B) Representative structures of library members. (C) Physicochemical properties of the library: MW = molecular weight; HBA = hydrogen-bond acceptor; HBD = hydrogen-bond donor; tPSA = total polar surface area.

(geomean REF = 1.0), for example acrylamide **1**, and these were taken forward for repeat qIT testing and mass spectrometry validation (Supporting Information Fig. S1). Pleasingly, four of those fragments both had reproducible qIT profiles and clearly mono-modified EV71 $3C^{pro}$ by intact protein mass spectrometry (Fig. 3B–D and Supporting Information Fig. S2). The glutathione selectivity of the four validated hit fragments ranged from REF = 8.5–24.3 and the compounds shared some common chemical features: acrylamides **1** and **2** both contain the same 1,3-thiazole core and methylene linker while acrylamides **3** and **4** have similar isoxazole motifs with more extended linkers. Encouragingly, all four hits are alkyl acrylamides which typically are associated with low levels of off-target reactivity and this is supported by their slow reactivity with glutathione[26].

2.2. *The hit fragments covalently bind to residue C147 of EV71 $3C^{pro}$ and accommodate a novel cryptic pocket*

To reveal the binding site of the cysteine-reactive fragments, we labelled recombinant EV71 $3C^{pro}$ with acrylamide fragments **1**–**4** and subjected the resulting complexes to crystallization trials. Unfortunately, the WT EV71 $3C^{pro}$-fragment complexes did not

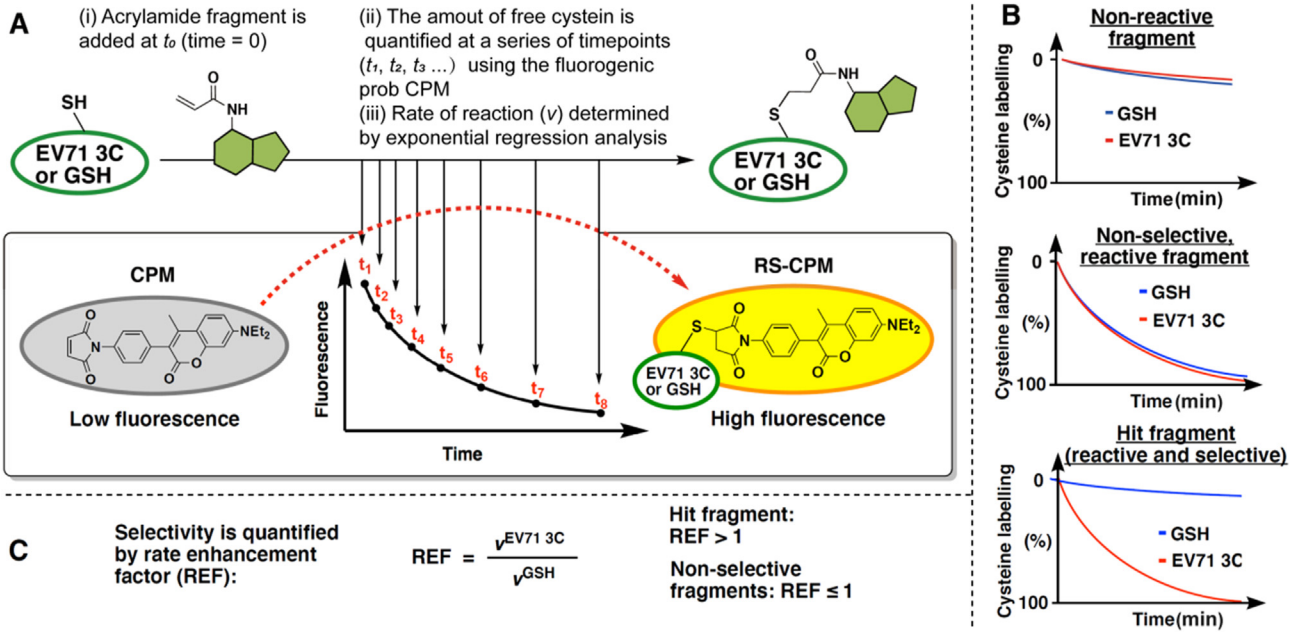

Figure 2 Quantitative irreversible tethering (qIT) screening platform. (A) Assay overview: The target thiol (5 μmol//L), EV71 $3C^{pro}$ or glutathione, is reacted with acrylamide fragments (0.5 mmol/L) under pseudo-first order conditions. Reaction progress is followed by discrete measurements of free target thiol concentration using the fluorogenic probe CPM and the rate of reaction (v) are derived from exponential regression analysis. (B) Fluorescence intensity is converted into percentage cysteine modification by normalizing to DMSO control = 0%, no thiol = 100%. Fragments are characterized as (i) non-reactive, (ii) reactive but non-selective or (iii) reactive and selective by comparing the reactivity profiles between EV71 $3C^{pro}$ and GSH. (C) Kinetic selectivity is quantified by the rate enhancement factor (REF) which is used to identify and prioritise hit compounds.

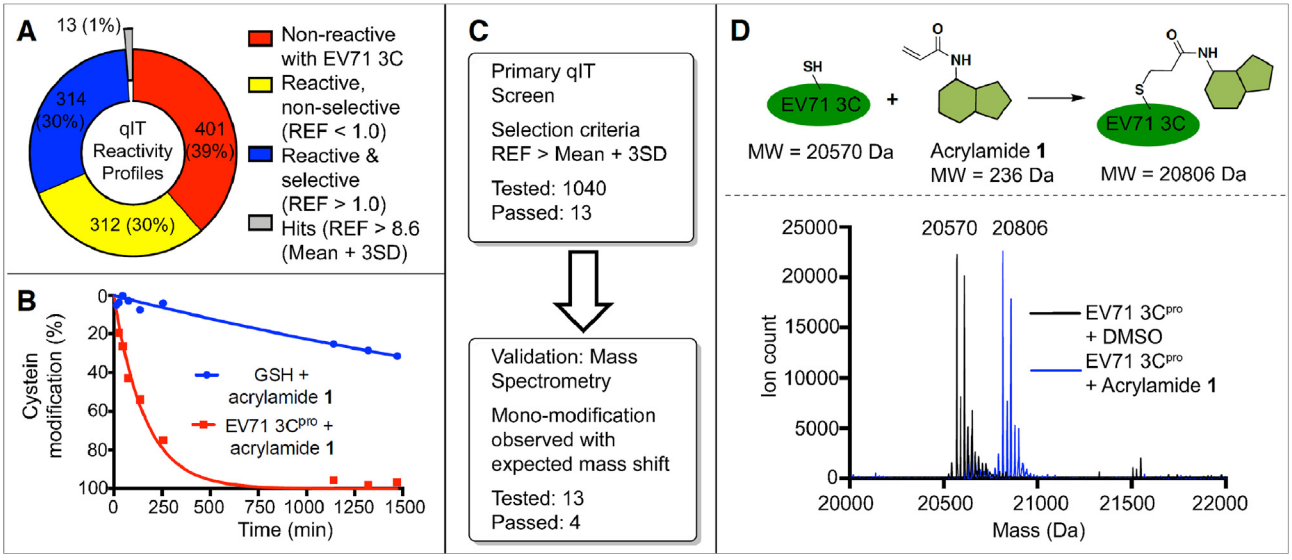

Figure 3 Screening cascade and hit validation. (A) Primary qIT screen summary: Pie chart shows number of fragments characterized as non-reactive, reactive but non-selective or reactive and selective. Hits have REF >3 standard deviations over the geometric mean. (B) Illustrative qIT data for acrylamide 1 (0.5 mmol/L) in reaction with EV71 3C^{pro} or glutathione (5 μmol/L). (C) Summary of screening cascade. (D) Illustrative intact protein mass spectrometry data for modification of EV71 3C^{pro} (5 μmol/L) reacting with acrylamide 1 (0.5 mmol/L for 750 min).

yield crystals so we employed a 3C^{pro} mutant construct bearing the H133G to expedite the structural studies. The H133G mutant has WT-level protease activity, containing a WT-like catalytic triad, and harbors the H133G mutation at the hinge region of the β-ribbon, which improves the flexibility of the β-ribbon[27]. Using the H133G mutant, we were able to determine crystal structures of 3C^{pro}−**1** and 3C^{pro}−**2** complexes; however, the structure determination of the other complexes remained unsuccessful.

Crystal structures of 3C^{pro}−**1** and 3C^{pro}−**2** complexes were solved to the resolution of 1.2−1.3 Å respectively, which provided atomic details of the 3C^{pro}−fragment interactions. We found that both fragments **1** and **2** bind to the same pocket on 3C^{pro}, with the acrylamide functionalities forming covalent bonds to C147 [bond length C (acrylamide)−S (C147) = 1.8 Å]. Unexpectedly, neither of the fragments occupy the central substrate pocket (S1−S4) of 3C^{pro}, as is observed for AG7088 and other characterized 3C^{pro} inhibitors[9]. Instead, the fragments accommodate a cryptic pocket on the other side of the catalytic cysteine, denoted the S′ pocket. To obtain bias-free structural insight, we calculated the composite omit maps for fragments **1** and **2**, which clearly show that the fragments are buried inside the S′ pocket and defines the orientation of the thiazole rings with the sulfur atoms contacting the bottom of the pocket (Fig. 4A−D). Comparing the binding of fragments **1** and **2**, we find that the trifluoromethyl and cyclohexane functionalities make less contact with protein and are associated with weaker electron density, hinting that the thiazole ring is the key pharmacophore.

2.3. Conformational rearrangement of the active site induced by covalent fragment binding

To our knowledge, the cryptic S′ pocket identified in our 3C^{pro}−fragment complexes has not been observed in the APO 3C^{pro} structures or other 3C^{pro}−inhibitor complex structures in the public database. By superimposing our structures with an EV71 3C^{pro}−AG7088 complex (PDB ID: 3R0F), we observed a large conformational rearrangement of a catalytically important loop 141−147 aa (Fig. 5). This loop harbors the catalytically critical residue C147 and constitutes the upper wall of the S1 pocket. While the 141−147 aa loop remains flexible in the absence of ligand, the binding of substrate (or inhibitor) can hold this loop in the catalytically active conformation, allowing residues G145 and C147 to form the oxyanion hole for the binding of tetrahedral intermediate anion.

The unusual conformation of the 141−147 aa loop in 3C^{pro}−**1** and 3C^{pro}−**2** structures led to a series of conformational rearrangements: (1) residue C147 side chain tilted towards the leaving group side of the active site. Comparing to EV71 3C^{pro}−AG7088 complex, displacement of the nucleophilic Sγ atom in our structures was 6.4 Å, indicating the geometry of the Ser-His-Asp catalytic triad was disrupted. Displacement of the NH group of G145 was 4.6 Å and displacement of NH of C147 was 1.8 Å, indicating the oxyanion hole could not form. (2) The upper wall of the S1 pocket (the most important pocket for substrate recognition) collapsed, and the size of the pocket became too narrow to accommodate the P1 residue. (3) The leaving group side pockets S1′ and S2′ disappeared, and a previously unobserved cryptic S′ pocket was generated. Residues constituting the cryptic S′ pocket involve I104, T106, H108, M109, M112, V114, F140, T142, A144, G145 and Q146. We marked the location of these residues constituting S′ pocket in a multiple sequence alignment of various picornavirus 3C^{pro}, most of which are conserved (Supporting Information Fig. S3).

2.4. The hit acrylamide fragments inhibit EV71 3C^{pro} and SARS-CoV-2 M^{pro} activity in vitro

To investigate which structural features of the thiazole-acrylamide fragments are key to binding, we tested analogues **5**, **6** and **7** for their kinetic binding profiles against 3C^{pro} using qIT (Table 1). Benzothiazole **5** retained potency (REF = 13.5) with a similar kinetic profile to thiazole **1**, further indicating that the thiazole motif drives the binding. Conversely, the N−H acrylamides **6** and

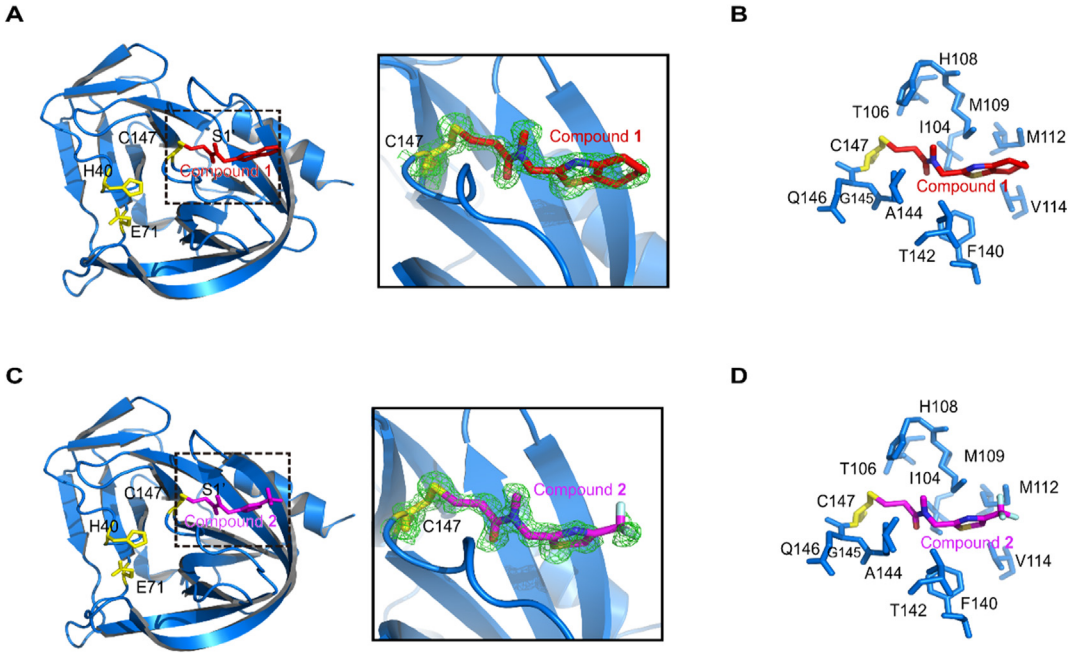

Figure 4 Crystal structures of EV71 $3C^{pro}$—cysteine reactive fragment complexes. (A) Ribbon model of EV71 $3C^{pro}$ (H133G) covalently linked to fragment 1. Catalytic triad C147—H40-E71 (yellow) and fragment 1 (red) are shown with stick model. Right, magnified view of the dashed line box on the left. A composite omit map (contour level = 1.5) is superimposed with the stick model of fragment 1. (B) Stick model of fragment 1 (red) binding the cryptic S′ pocket (blue) identified on the leaving group side of EV71 $3C^{pro}$ active site. (C) Ribbon model of EV71 $3C^{pro}$ (H133G) covalently linked to fragment 2. Catalytic triad (yellow) and fragment 2 (magenta) are shown with stick model. Right, magnified view of the dashed line box on the left. A composite omit map (contour level = 1.5) is superimposed with the stick model of fragment 2. (D) Stick model of fragment 2 (magenta) binding the cryptic S′ pocket (blue) identified on the leaving group side of EV71 $3C^{pro}$ active site.

7 reacted with $3C^{pro}$ >50 times more slowly than the parent acrylamide **1**, indicating that alkyl functionalization of the amide nitrogen is required for efficient binding. Indeed, tolerance of the cyclopropane ring of acrylamide **5** indicates that larger substituents may be introduced here and based on the crystal structures of fragments **1** and **2**, this represents a suitable vector for fragment growth towards the canonical binding groove.

Next, we employed a fluorogenic peptide-based $3C^{pro}$ protease activity assay to assess biochemical potency of the acrylamides. In accordance with the qIT data, acrylamides **1**—**5** all demonstrated concentration dependent inhibition of $3C^{pro}$ with modest potency (IC_{50} = 30—230 μmol/L) that is typical of unoptimized fragments.

With the emergence of SARS-CoV-2 as a threat to global public health, we sought to determine if our $3C^{pro}$-selective fragments could be re-purposed towards this second plus strand RNA virus. Given that $3C^{pro}$ and M^{pro} are both cysteine proteases that share similar chymotrypsin-folds, we hypothesized that our acrylamide fragments might also be effective against M^{pro}. The first examples of covalent SARS-CoV-2 M^{pro} inhibitors have already emerge[19,28,29], but novel acrylamide-based M^{pro} inhibitor scaffolds remain highly desirable. Accordingly, we incubated each fragment with SARS-CoV-2 M^{pro} and used intact protein mass spectrometry to check for covalent modification (Table 1 and Supporting Information Fig. S4). Encouragingly, acrylamides **1**, **3** and **4** showed partial modification while fragments **2** and **5** both labelled M^{pro} to completion. Using an M^{pro} activity assay, we validated these results and found that the inhibitory potency against M^{pro} is overall greater than $3C^{pro}$ (IC_{50} = 10—60 μmol/L), with acrylamides **2** and **5** being the most potent against either proteases. To test selectivity of compounds **1**—**5**, we investigated their potency against another SARS-CoV-2 cysteine protease, the papain-like protease (PL^{pro}). PL^{pro} contains a catalytic triad C111—H272-D286 at the active site, but its substrate binding pockets are distinct from M^{pro} or $3C^{pro}$. The S1—S2 subpockets of PL^{pro} are very narrow which can only accommodate glycine residues; hence, it presents a good control for compound selectivity assessment. Only fragment **4** exhibits moderate efficacy against PL^{pro} (IC_{50} = 33.47 μmol/L), and all other fragments were ineffective. Of note, fragments **2** and **5** potent against M^{pro} cannot inhibit PL^{pro}, suggesting evident selectivity. Although other covalent fragment inhibitors of M^{pro} have recently been disclosed[19], to our knowledge, our fragments represent the first examples of acrylamide-based fragment inhibitors of M^{pro}. Acrylamide-based electrophiles offer low pharmacological risk as indicated by their widespread clinical use, emphasizing the development potential of fragments **2** and **5**. To better understand what role the acrylamide warhead plays in the fragment binding, we synthesized analogues of fragment **2** in which the acrylamide warhead was substituted with a vinyl sulfonamide, chloroacetamide or acrylate electrophile (Supporting Information Fig. S5). Interestingly, although these three alternative warheads have higher intrinsic reactivity than acrylamides, they did not increase the potency, suggesting that the acrylamide plays a key structural role in the covalent modification.

2.5. *Mechanism of the fragment efficacy against M^{pro}*

To reveal the inhibitory mechanism of these fragments against M^{pro}, we determined the crystal structure of M^{pro} with **2** and with **5** (Fig. 6). The crystals of M^{pro}—**5** complex diffracted to 2.3 Å, had a $P2_12_12_1$ space group and contained one M^{pro} dimer in the

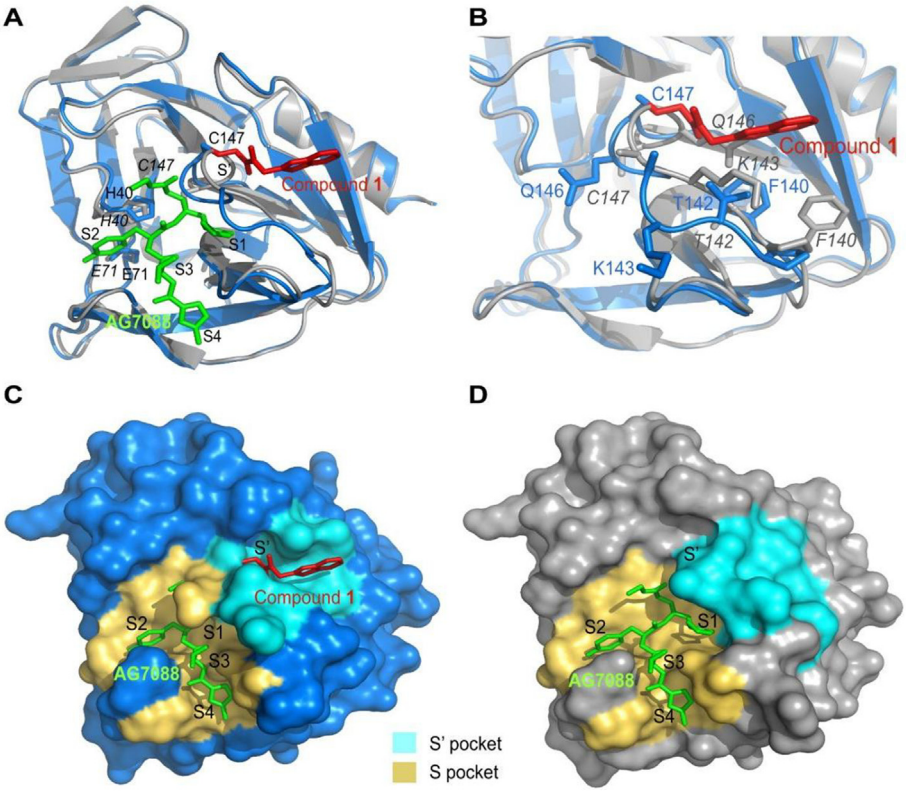

Figure 5 Fragment binding induces significant conformational rearrangement at the active site and substrate pockets. (A) The structure of EV71 $3C^{pro}$−**1** complex (blue) superimposed with the structure of EV71 $3C^{pro}$−AG7088 complex, revealing large conformational changes of a catalytically important loop 141−147 aa. Fragment **1** (red) and AG7088 (green) are shown with stick models. (B) Zoom in view of the 141−147 aa loop. Residues on the loop are shown with stick models. (C) Molecular surface of $3C^{pro}$−**1** complex. AG7088 is modeled to substrate binding pockets of $3C^{pro}$ *via* structure superimposition. Due to **1** binding induced conformational changes, S1 pocket collapsed and it cannot accommodate the P1 residue. Substrate pockets S1−S5 are highlighted in yellow, the cryptic pocket on leaving group side S′ is highlighted in cyan. (D) Molecular surface of $3C^{pro}$−AG7088 complex. AG7088 occupies substrate pockets S1−S5, highlighted in yellow; the residues forming the cryptic pocket on leaving group side S′ are highlighted in cyan.

asymmetric unit (ASU). Structural comparison of two monomers in ASU gave a root-mean-squared deviation (RMSD) of 0.73 Å. The crystals of the M^{pro}−**2** complex diffracted to 1.8 Å, had a C2 space group and contained a single M^{pro} molecule in the ASU. It formed a typical M^{pro} dimer with the symmetry mate (*-x*, *-y*, *-z*), suggesting two M^{pro} protomers have identical conformation.

We identified electron density of compound **5** connecting to the active site cysteine C145 in both M^{pro} monomers in ASU. For the M^{pro}−**2** complex, we observed electron density of **2** connecting to the active site residue C145. We generated the polder maps for the above structures with the compound **2** or **5** omitted (Supporting Information Fig. S6). Positive densities clearly delineated the structure of compounds **2** and **5**, confirming the presence of the fragments.

In the active site, the acrylamide moiety of **5** forms a covalent bond with C145 (Fig. 6A and B). While the R′ group (benzothiazole) of **5** is accommodated in the deep S2 pocket of M^{pro}, the cyclopropane group is exposed to solvent. The benzothiazole/S2 pocket interaction is mainly hydrophobic, involving residues H41, M49, Q189 and M165. The stacking of the H41 imidazole side chain with the benzothiazole moiety stabilizes the fragment.

Similarly, the acrylamide moiety of **2** is covalently linked to residue C145 (Fig. 6C and D). Owing to the high resolution of M^{pro}−**2** structure and unambiguous electron density for the fragment, we were able to build the fragment more accurately. We measured the length of the S−C bond between C145 and compound **2** to be 1.8 Å, very close to the average length of single S−C bond, 1.82 Å[30]. The trifluoromethyl thiazole moiety of compound **2** is also accommodated by the S2 pocket. While the trifluoromethyl group touches the apex of the pocket and the thiazole ring π-stacks with the side chain of H41. Both two and five occupy only the S1′ and S2 subsites, implying substantial opportunity to develop these fragments.

While picornavirus $3C^{pro}$ functions as a monomer, coronavirus M^{pro} is an obligate dimer. An additional C-terminal domain in M^{pro} stabilizes dimerization and the dimerization interface is essential to maintain the active conformation. We next investigated the oligomerization state of the five M^{pro}-fragment complexes using size-exclusion chromatography (Supporting Information Fig. S7). As expected, M^{pro}−**2**, M^{pro}−**3** and M^{pro}−**4** eluted as dimers with calculated molecular masses of 45.7, 45.7 and 47.9 kDa, respectively. Interestingly, however, M^{pro}−**5** eluted as a monomer. The calculated molecular mass of M^{pro}−**5** is 25.3 kDa, whereas the theoretical molecular mass of M^{pro} monomer is 33.7 kDa. The retention volume of M^{pro}−**1** lies between the monomeric and dimeric forms, with a calculated

Table 1 Biochemical characterization of acrylamide fragments.

Compd.	Structure	EV71 $3C^{pro}$				SARS-CoV-2		
						M^{pro}		PL^{pro}
		qIT (K_{obs}/[I] (L/mol·s))		REF	*In vitro* inhibition IC_{50} (μmol/L)	Covalent labelling by MS after 18 h	*In vitro* inhibition IC_{50} (μmol/L)	*In vitro* inhibition IC_{50} (μmol/L)
		GSH	EV71 3C					
1	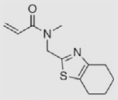	0.009	0.207	24.3	63.6	93% +235 Da	21.4	>100
2	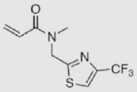	0.012	0.103	8.5	40.7	100% +251 Da	10	>100
3	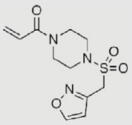	0.010	0.110	10.5	224.6	18% +284 Da	56.6	>100
4	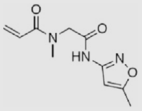	0.014	0.230	16.3	68.3	75% +224 Da	20.2	33.5
5	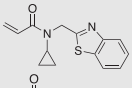	0.016	0.222	13.5	30.1	100% +260 Da	17	>100
6	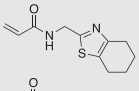	<0.001	0.004	na	–	–	–	–
7	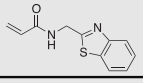	<0.001	<0.001	na	–	–	–	–

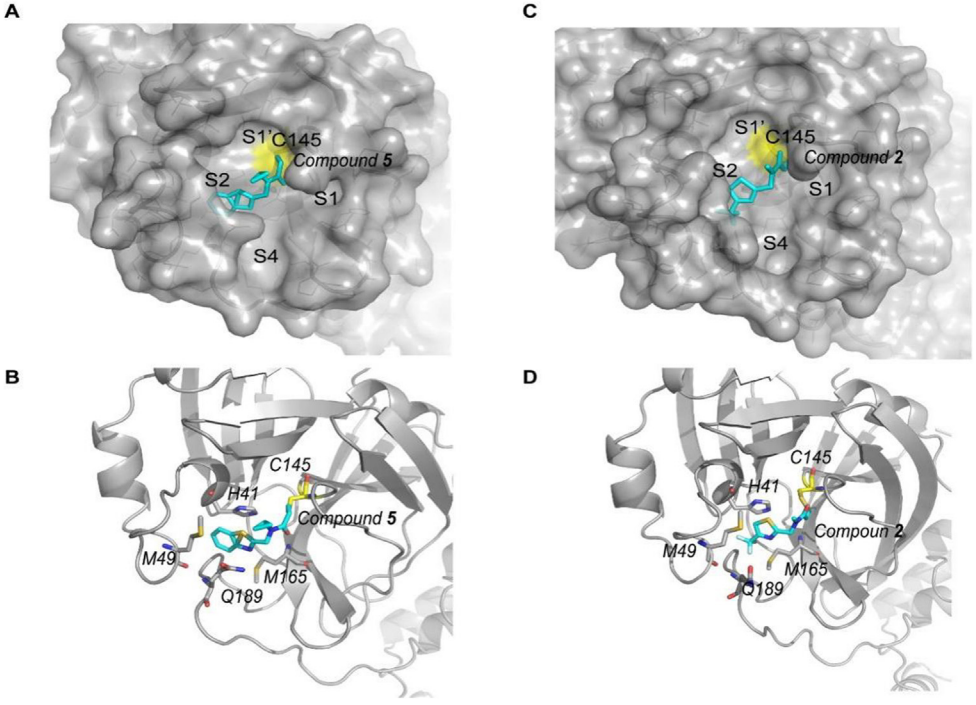

Figure 6 Structure of SARS-CoV-2 M^{pro} complexed with compounds **2** and **5.** (A) Surface plot of SARS-CoV-2 M^{pro} complexed by compound **5** (cyan). Compound **5** occupies pockets S1′ and S2. (B) Ribbon model of SARS-CoV-2 M^{pro}—**5**. Residues surrounding the benzothiazole moiety of five are shown with stick model. (C) Surface plot of SARS-CoV-2 M^{pro} complexed with **2** (cyan). The trifluoromethyl thiazole moiety of **2** occupies the S2 pocket. (D) Ribbon model of SARS-CoV-2 M^{pro}—**2**. Residues surrounding the trifluoromethyl thiazole moiety are shown with stick model.

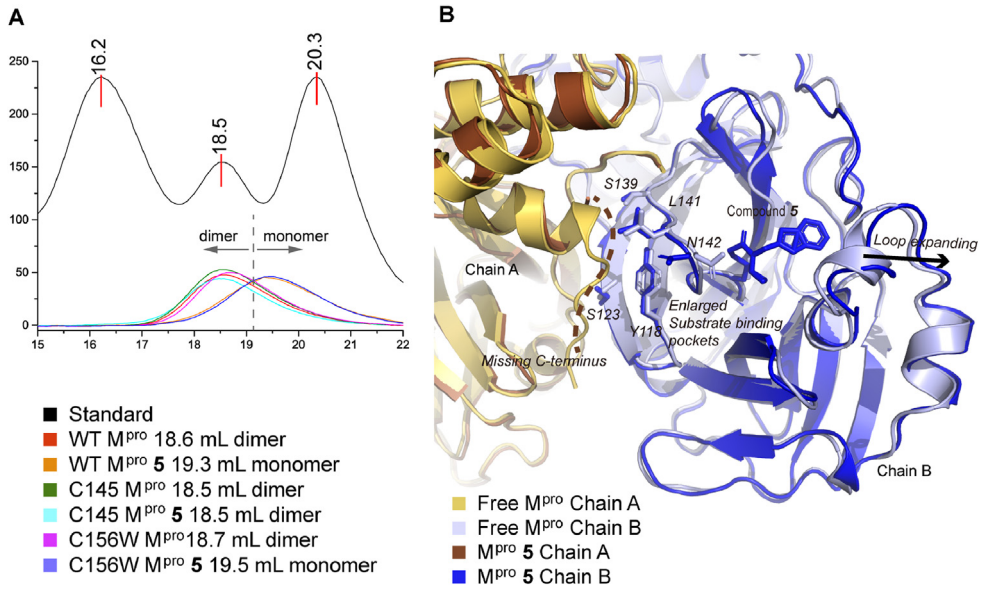

Figure 7 Inhibitory mechanism of **5**. (A) Size-exclusion chromatography analyses two M^{pro} mutants C145A and C156A, the unliganded and labelled with **5**. Elution volume of standards and M^{pro} variants are indicated. (B) Structural comparison of the unliganded SARS-CoV-2 M^{pro} dimer (PDB ID: 6YB7) with M^{pro}—**5** dimer. The labelling with **5** expanded the substrate binding pockets. The conformation of several residues (shown with stick model) at the dimer interface were altered. Loops expanding outward are indicated with the arrow. The missing C-terminal region of M^{pro}—**5** chain A is indicated with the dashed line.

molecular mass of 37.6 kDa. This suggests the dimerization was partially impaired.

2.6. *Unique inhibitory mechanism of compound 5*

To further validate the effects of **5** on M^{pro} dimerization, we tested the oligomerization state of two M^{pro} mutants, C145A and C156W in the absence and presence of ligand. As well as the active site cysteine (C145), C156 is also surface exposed and potentially reactive so the C156W mutant served as a control mutation. Indeed, mutant C156W behaved similarly to the wild-type enzyme: apo-M^{pro} C156W eluted as dimers in size-exclusion chromatography, whilst labelling with **5** retarded M^{pro} elution to that expected for a monomer (Fig. 7A). By contrast, mutant C145A remained dimeric irrespective of the presence of **5**. Given that the C145A mutation prevents the labelling of the active site cysteine, these results clearly indicate that the labelling of C145 by acrylamide **5** drives dimer disruption.

Our crystallographic data provides further insights into the inhibition mechanism. Although M^{pro}—**5** forms dimers in crystal lattices, these are notably different from authentic M^{pro} dimers: (1) Most published M^{pro} dimers have 2-fold symmetry between two protomers, but M^{pro}—**5** protomers exhibit marked difference, RMSD = 0.73 Å. The structure of each M^{pro}—**5** protomer is also notably different from the free enzyme (PDB ID: 6YB7), r.m.s.d = 0.71—0.78 Å. In this regard, M^{pro}-**2** is more similar to the free enzyme. The structure of M^{pro}—**2** dimer has 2-fold symmetry and each protomer is highly similar to the free enzyme, r.m.s.d = 0.22 Å. (2) The binding of **5** enlarged the substrate binding pockets and affected the nearby regions (Fig. 7B). Compared to the free enzyme, the loops surrounding compound **5** have expanded to make room for the benzothiazole motif. This induced conformational changes of several residues and regions at the dimerization interface. In the chain A of the M^{pro}—**5** dimer, the extreme C-terminal region at the dimer interface is disordered, which is likely caused by the labelling of compound **5** on C145. The fragment induced conformational alterations may contribute to the destabilization of M^{pro}—**5** dimers. In summary, we found that **5** has at least two mechanisms of action to inhibit M^{pro}: (1) covalently linking to the catalytically essential cysteine and occupying the substrate binding pockets; (2) destabilizing the dimerization of M^{pro}.

To further elucidate how M^{pro} dimerization is disrupted by modification with compound **5**, we ran molecular dynamics simulations[31,32] comparing WT M^{pro} and WT M^{pro}—**5** system (Supporting Information Fig. S8 left). We found that compound **5** destabilizes the steady-state dimer interaction energy by 80.6 kcal/mol (Fig. S8 right).

2.7. *Data availability*

Final coordinates and structure factors of EV71 $3C^{pro}$ complexed by compounds **2** and **1** and SARS-CoV-2 M^{pro} complexed by compounds **2** and **5** have been deposited in the Protein Data Bank under the accession codes: 7WYL, 7WYM, 7WYO and 7WYP.

3. Conclusions

We have identified acrylamide fragments that target both the EV71 $3C^{pro}$ and SARS-CoV-2 M^{pro}, and inhibit their activity by covalently reacting with their catalytic cysteines. Importantly, some of these hit fragments cause profound structural rearrangements of each protease: in the case of EV71 $3C^{pro}$ a new subsite pocket is formed at the expense of the normal active site architecture whilst with M^{pro} key structural features required for dimerization are distorted preventing formation of the active dimeric unit. The discovery of these conformational change-based mechanisms of action on covalent fragment binding demonstrates the utility of solution-based

screening methodologies as an alternative to crystallographic fragment screening in which structural rearrangements are unlikely. The fragment-like nature of the inhibitors described herein enables them to bind diverse targets in different modes as exemplified by the distinct binding poses of compound **2** in complex with EV71 $3C^{pro}$ and after repurposing against SARS-CoV-2 M^{pro}. As such, these molecules lack specificity and without further development are anticipated to have significant off-target activity and toxicity in more complex systems. Nevertheless, these hit ligands provide excellent candidates for development of potent protease inhibitors by structure-based design.

Acknowledgments

This work was supported by grants from Chinese Academy of Medical Sciences (CAMS) Innovation Fund for Medical Sciences (2021-I2M-1-037, China), National Key Research and Development Program of China (2016YFD0500300) and the CRP-ICGEB Research Grant 2019 (CRP/CHN19-02, China); This work was supported by grants from the Institute of Chemical Biology (Imperial College London, UK), the UK Engineering and Physical Sciences Research Council (Studentship award EP/F500416/1, UK) and The Imperial College COVID19 Research Fund. The crystallization facility at Imperial College was funded by BBSRC (BB/D524840/1, UK) and the Wellcome Trust (202926/Z/16/Z, UK). Finally, we also thank Ms Liu siqi for help with EV71 3C protein expression and crystallization.

Author contributions

Sheng Cui and David J. Mann designed the study. Sheng Cui, David J. Mann, Bo Qin, Gregory B. Craven and Pengjiao Hou solved the structure and wrote the paper. Bo Qin, Gregory B. Craven, Pengjiao Hou, Julian Chesti, Xinran Lu, Emma S. Child, Rhodri M. L. Morgan, Wenchao Niu, Lina Zhao and Alan Armstrong performed experiments. Sheng Cui, David J. Mann, Bo Qin, Gregory B. Craven and Pengjiao Hou analyzed the data and revised the paper. All authors reviewed the results and approved the final version of the manuscript.

Conflict of interest

The authors declare no conflicts of interest.

Appendix A. Supporting information

Supporting data to this article can be found online at https://doi.org/10.1016/j.apsb.2022.06.002.

References

1. Poltronieri P, Sun B, Mallardo M. RNA Viruses: RNA roles in pathogenesis, coreplication and viral load. *Curr Genom* 2015;**16**:327−35.
2. Woolhouse MEJ, Brierley L. Epidemiological characteristics of human-infective RNA viruses. *Sci Data* 2018;**5**:180017.
3. Lee KY. Enterovirus 71 infection and neurological complications. *Korean J Pediatr* 2016;**59**:395−401.
4. Li R, Liu L, Mo Z, Wang X, Xia J, Liang Z, et al. An inactivated enterovirus 71 vaccine in healthy children. *N Engl J Med* 2014;**370**:829−37.
5. Nhan LNT, Hong NTT, Nhu LNT, Nguyet LA, Ny NTH, Thanh TT, et al. Severe enterovirus A71 associated hand, foot and mouth disease, Vietnam, 2018: preliminary report of an impending outbreak. *Euro Surveill* 2018;**23**:1800590.
6. Lin JY, Kung YA, Shih SR. Antivirals and vaccines for enterovirus A71. *J Biomed Sci* 2019;**26**:65.
7. Sun D, Chen S, Cheng A, Wang M. Roles of the Picornaviral 3C proteinase in the viral life cycle and host cells. *Viruses* 2016;**8**:82.
8. Wang HM, Liang PH. Picornaviral 3C protease inhibitors and the dual 3C protease/coronaviral 3C-like protease inhibitors. *Expert Opin Ther Pat* 2010;**20**:59−71.
9. Patick AK, Binford SL, Brothers MA, Jackson RL, Ford CE, Diem MD, et al. *In vitro* antiviral activity of AG7088, a potent inhibitor of human rhinovirus 3C protease. *Antimicrob Agents Chemother* 1999;**43**:2444−50.
10. Hayden FG, Turner RB, Gwaltney JM, Chi-Burris K, Gersten M, Hsyu P, et al. Phase II, randomized, double-blind, placebo-controlled studies of ruprintrivir nasal spray 2-percent suspension for prevention and treatment of experimentally induced rhinovirus colds in healthy volunteers. *Antimicrob Agents Chemother* 2003;**47**:3907−16.
11. Hu B, Guo H, Zhou P, Shi ZL. Characteristics of SARS-CoV-2 and COVID-19. *Nat Rev Microbiol* 2021;**19**:141−54.
12. Classification of Omicron (B.1.1.529): SARS-CoV-2 variant of concern. Available from: https://www.who.int/news/item/26-11-2021-classification-of-omicron-(b.1.1.529)-sars-cov-2-variant-of-concern.
13. Anand K, Ziebuhr J, Wadhwani P, Mesters JR, Hilgenfeld R. Coronavirus main proteinase (3CLpro) structure: basis for design of anti-SARS drugs. *Science* 2003;**300**:1763−7.
14. Ratia K, Saikatendu KS, Santarsiero BD, Barretto N, Baker SC, Stevens RC, et al. Severe acute respiratory syndrome coronavirus papain-like protease: structure of a viral deubiquitinating enzyme. *Proc Natl Acad Sci U S A* 2006;**103**:5717−22.
15. Singh J, Petter RC, Baillie TA, Whitty A. The resurgence of covalent drugs. *Nat Rev Drug Discov* 2011;**10**:307−17.
16. Lee CS, Rattu MA, Kim SS. A review of a novel, Bruton's tyrosine kinase inhibitor, ibrutinib. *J Oncol Pharm Pract* 2016;**22**:92−104.
17. Butterworth S, Cross DAE, Finlay MRV, Ward RA, Waring MJ. The structure-guided discovery of osimertinib: the first U.S. FDA approved mutant selective inhibitor of EGFR T790M. *MedChemComm* 2017;**8**:820−2.
18. Jackson PA, Widen JC, Harki DA, Brummond KM. Covalent modifiers: a chemical perspective on the reactivity of α,β-unsaturated carbonyls with thiols *via* hetero-michael addition reactions. *J Med Chem* 2017;**60**:839−85.
19. Douangamath A, Fearon D, Gehrtz P, Krojer T, Lukacik P, Owen CD, et al. Crystallographic and electrophilic fragment screening of the SARS-CoV-2 main protease. *Nat Commun* 2020;**11**:5047.
20. Craven GB, Affron DP, Allen CE, Matthies S, Greener JG, Morgan RML, et al. High-throughput kinetic analysis for target-directed covalent ligand discovery. *Angew Chem Int Ed Engl* 2018;**57**:5257−61.
21. Craven GB, Affron DP, Kösel T, Wong TLM, Jukes ZH, Liu CT, et al. Multiparameter kinetic analysis for covalent fragment optimization by using quantitative irreversible tethering (qIT). *Chembiochem* 2020;**21**:3417−22.
22. Graham F. Daily briefing: pfizer's COVID pill looks promising. *Nature* 08 November 2021. Available from: https://doi.org/10.1038/d41586-021-03379-5.
23. Zhao Y, Fang C, Zhang Q, Zhang R, Zhao X, Duan Y, et al. Crystal structure of SARS-CoV-2 main protease in complex with protease inhibitor PF-07321332. *Protein Cell* 2022;**13**:689−93.
24. Wu KD, Chen GS, Liu JR, Hsieh CE, Chern JW. Acrylamide functional group incorporation improves drug-like properties: an example with EGFR inhibitors. *ACS Med Chem Lett* 2019;**10**:22−6.
25. Congreve M, Carr R, Murray C, Jhoti H. A 'rule of three' for fragment-based lead discovery?. *Drug Discov Today* 2003;**8**:876−7.
26. Flanagan ME, Abramite JA, Anderson DP, Aulabaugh A, Dahal UP, Gilbert AM, et al. Chemical and computational methods for the

characterization of covalent reactive groups for the prospective design of irreversible inhibitors. *J Med Chem* 2014;**57**:10072−9.
27. Wang J, Fan T, Yao X, Wu Z, Guo L, Lei X, et al. Crystal structures of enterovirus 71 3C protease complexed with rupintrivir reveal the roles of catalytically important residues. *J Virol* 2011;**85**: 10021−30.
28. Dai W, Zhang B, Jiang XM, Su H, Li J, Zhao Y, et al. Structure-based design of antiviral drug candidates targeting the SARS-CoV-2 main protease. *Science* 2020;**368**:1331−5.
29. Hoffman RL, Kania RS, Brothers MA, Davies JF, Ferre RA, Gajiwala KS, et al. Discovery of ketone-based covalent inhibitors of coronavirus 3CL proteases for the potential therapeutic treatment of COVID-19. *J Med Chem* 2020;**63**:12725−47.
30. Trinajstić N. Calculation of carbon-sulphur bond lengths. *Tetrahedron Lett* 1968;**9**:1529−32.
31. Khan A, Heng W, Wang Y, Qiu J, Wei X, Peng S, et al. *In silico* and *in vitro* evaluation of kaempferol as a potential inhibitor of the SARS-CoV-2 main protease (3CLpro). *Phytother Res* 2021;**35**:2841−5.
32. Khan A, Umbreen S, Hameed A, Fatima R, Zahoor U, Babar Z, et al. *In silico* mutagenesis-based remodelling of SARS-CoV-1 peptide (ATLQAIAS) to inhibit SARS-CoV-2: structural-dynamics and free energy calculations. *Interdiscip Sci* 2021;**13**:521−34.